

# Femtojoule femtosecond all-optical switching in lithium niobate nanophotonics

Qiushi Guo<sup>1,4</sup>, Ryoto Sekine<sup>® 1,4</sup>, Luis Ledezma<sup>® 1,2,4</sup>, Rajveer Nehra<sup>® 1</sup>, Devin J. Dean<sup>3</sup>, Arkadev Roy<sup>1</sup>, Robert M. Gray<sup>1</sup>, Saman Jahani<sup>® 1</sup> and Alireza Marandi<sup>® 1</sup> ⊠

Optical nonlinear functions are crucial for various applications in integrated photonics, including all-optical information processing<sup>1</sup>, photonic neural networks<sup>2,3</sup> and on-chip ultrafast light sources<sup>4,5</sup>. However, the weak native nonlinearity of most nanophotonic platforms has imposed barriers for such functions by necessitating large driving energies, high-O cavities or integration with other materials with stronger nonlinearity. Here we effectively utilize the strong and instantaneous quadratic nonlinearity of lithium niobate nanowaveguides for the realization of cavity-free all-optical switching. By simultaneous engineering of the dispersion and quasi-phase matching, we design and demonstrate a nonlinear splitter that can achieve ultralow switching energies down to 80 fJ, featuring a fastest switching time of ~46fs and a lowest energy-time product of  $3.7 \times 10^{-27}$  Js in integrated photonics. Our results can enable on-chip ultrafast and energy-efficient all-optical information processing, computing systems and light sources.

Photons are known to be excellent information carriers. Yet, the quest for all-optical information processing—a technology that can potentially eliminate the limitations on the bandwidth and energy consumption of electronic and opto-electronic systems—is generally deemed to be challenging because optical nonlinearities are usually weak. All-optical switching using cubic  $(\chi^{(3)})$  nonlinearities<sup>6,7</sup> and saturable absorption<sup>8-10</sup> in semiconductor materials typically requires pulse energies on the order of picojoules or beyond. Such energy requirements hinder their widespread utilization for any applications, as they necessitate bulky and power-hungry light sources. To lower the energy requirement of all-optical switching, one approach consists of enhancing the optical nonlinearity in optical cavities. However, this enhancement is accompanied by a cavity photon lifetime, which unavoidably increases the switching times and typically leads to low bandwidths of up to tens of gigahertz<sup>1,11–16</sup>. Therefore, all-optical switching in solid-state photonic platforms faces a performance trade-off between the energy per bit and the switching time<sup>17</sup>, making the energy-time product an apt figure of merit<sup>18</sup>. A promising path towards a better energy-time product is the utilization of stronger and instantaneous nonlinearities, such as the quadratic nonlinearity ( $\chi^{(2)}$ ).

Compared to the  $\chi^{(3)}$  nonlinearity,  $\chi^{(2)}$  nonlinearity in noncentrosymmetric materials requires lower light intensities by many orders of magnitude. When the phase-matching condition is achieved and in the absence of substantial dispersion, nonlinear optical interactions can grow substantially as a function of propagation length, thus circumventing the need for resonant enhancement and compromising switching speed. Recently, thin-film lithium niobate (TFLN) has emerged as a promising integrated

photonic platform. TFLN-based nanophotonic waveguides exhibit strong  $\chi^{(2)}$  nonlinearity and a high normalized nonlinear frequency conversion efficiency in the continuous wave (c.w.) regime (>1,000% W<sup>-1</sup> cm<sup>-2</sup>)<sup>19–22</sup> that is not easily attainable in bulk material platforms, thanks to the strong spatial confinement of the waveguide modes as well as quasi-phase matching (QPM). Additionally, the tight spatial confinement of the waveguide modes allows dispersion engineering<sup>23–25</sup>, which enables temporal confinement of interacting waves over long interaction lengths, leading to further enhancement of the nonlinear processes using ultrashort pulses.

In this Letter we achieve cavity-free all-optical switching in an integrated LN nonlinear splitter, which cascades two distinct phase-matched  $\chi^{(2)}$  nonlinear processes: second-harmonic generation (SHG) and degenerate optical parametric amplification (DOPA). Simultaneously, dispersion engineering of our device allows spatio-temporal confinement of the pulses over the length of the device, leading to ultralow-energy (femtojoule) and ultrafast (femtosecond) all-optical switching with a high extinction ratio. It is worth noting that the design and operating principle of our device are fundamentally different from the all-optical switches based on nonlinear directional couplers in micro-waveguides<sup>26</sup>. In those devices, the switching originates from the perturbation of the evanescent coupling due to phase-mismatched  $\chi^{(2)}$  nonlinearity and self-phase modulation of the input pulses<sup>27,28</sup>, whereas in our device the switching mechanism arises from the phase-matched wavelength conversions and the spectral selectivity of the linear directional coupler, leading to a record-level performance (Supplementary Section I provides a detailed comparison).

The main element of our all-optical switch is a QPM-engineered LN nanophotonic waveguide. Figure 1a illustrates the concept of this QPM engineering. A uniform periodically poled LN waveguide (with periodicity  $\Lambda$ ) is perturbed by a 'poling defect', that is, an isolated ferroelectric domain of length  $L=\Lambda$  in the middle of the waveguide. Although the poling period is designed for phase-matched SHG, the poling defect locally changes the phase relationship between the first-harmonic (FH) and the second-harmonic (SH) waves by  $\Delta\phi = \phi_{2\omega} - 2\phi_{\omega} = \pi$  (ref. <sup>29</sup>). Because the direction of power flow between the FH and the SH is dependent on the relative phase between them, the  $\pi$  phase shift due to the poling defect switches the nonlinear process from SHG to DOPA, in which the generated SH serves as the pump to amplify the FH.

In addition to the QPM-engineered main waveguide, our all-optical switch is composed of a neighbouring linear directional coupler, as sketched in Fig. 1b,d. The linear directional coupler evanescently couples out most (85%) of the FH, while leaving most of SH freely propagating in the main waveguide. This whole device

<sup>1</sup>Department of Electrical Engineering, California Institute of Technology, Pasadena, CA, USA. <sup>2</sup>Jet Propulsion Laboratory, California Institute of Technology, Pasadena, CA, USA. <sup>3</sup>Department of Applied Physics, Cornell University, Ithaca, NY, USA. <sup>4</sup>These authors contributed equally: Qiushi Guo, Ryoto Sekine, Luis Ledezma. <sup>™</sup>e-mail: marandi@caltech.edu

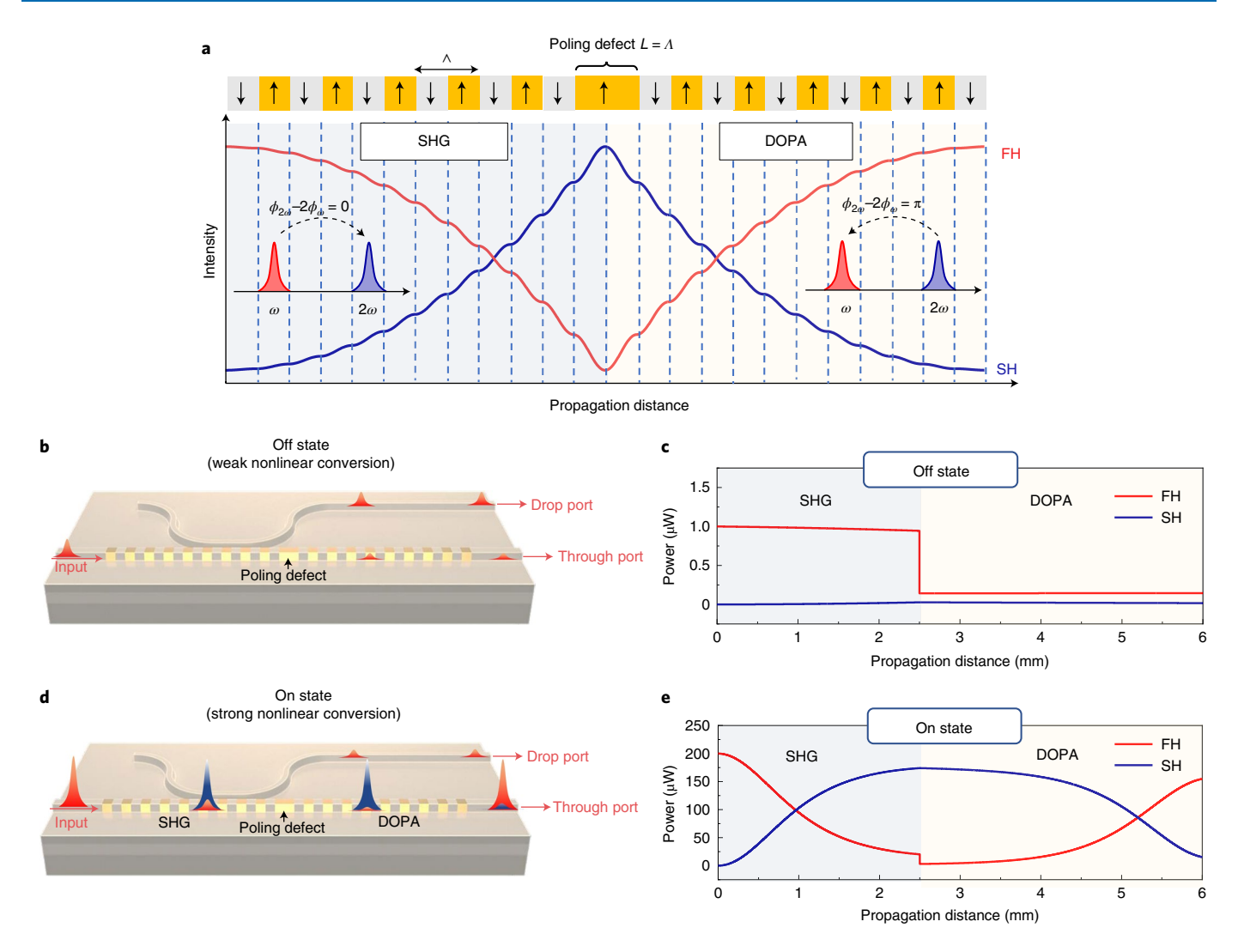


**Fig. 1** Device design and operating principle. **a**, Illustration of QPM engineering in a periodically poled lithium niobate (PPLN) waveguide. The poling defect (a longer ferroelectric domain with length  $L=\Lambda$ ) shifts the phase difference between the FH and SH by π. As a result, the poling defect switches the SHG to DOPA in the second half of the PPLN waveguide. The insets illustrate the phase relation and the direction of energy transfer between the FH and the SH. **b**, Schematic of the integrated nonlinear splitter device and its operation in the off state when the input FH pulse energy is low. **c**, Simulated evolution of the FH and SH optical power along the main waveguide for the off state, in which the transmittance of the FH is low (15%). **d**, Schematic of the integrated nonlinear splitter device and its operation in the on state when the input pulse energy is high. **e**, Simulated evolution of the FH and SH optical power along the main waveguide for the on state, in which the transmittance of the FH is high (85%). The simulations in **c** and **e** assume an input pulse of 46 fs at 2,090 nm and device parameters of a 2.5-mm-long SHG region, a 3.5-mm-long DOPA region and 85% outcoupling of the FH by the directional coupler.

exhibits a strongly intensity-dependent splitting ratio. When the input FH intensity is low (in the off state shown in Fig. 1b), most of the input FH does not convert to SH, and hence is directed by the linear coupler to the drop port. This is illustrated by the simulated power evolution of both the FH and the SH in the main waveguide in Fig. 1c. In this off state, the transmittance of the FH in the main waveguide (through port) is low. However, when the input FH intensity is high (or in the on state as shown in Fig. 1d,e), due to the efficient SHG at the beginning of the waveguide, most of the FH can convert to the SH, which remains in the main waveguide after passing through the coupler, and negligible FH is directed to the drop port. In the second half of the main waveguide, the poling defect switches the SHG process to DOPA, through which most of the SH converts back to the FH. As shown in Fig. 1e, in the on state, the device favours transmission of the FH to the through port, because most of the input pulse energy can be 'stored' in (that is, converted to) the SH, which is unaffected by the linear coupler. Because the

FH transmission strongly depends on the input pulse energy of the FH, the intensity-dependent nonlinear splitter functions as an all-optical switch.

We fabricated the nonlinear splitter on a 700-nm-thick X-cut MgO-doped LN thin film on a 2- $\mu$ m-thick SiO<sub>2</sub> layer on top of a LN substrate (NANOLN). Details about the periodic poling, the waveguide patterning and etching are provided in the Methods. As shown in the scanning electron microscope (SEM) image in Fig. 2a and the atomic force microscope (AFM) image in Fig. 2b, the Ar-based dry etching process yields smooth waveguide sidewalls (with surface roughness of ~1 nm) and a sidewall angle of ~60°. The top width of the main waveguide and the etching depth are measured to be 1,650 nm and 350 nm, respectively, with an error of  $\pm 5$  nm. In Supplementary Section VII, we discuss how the variation of the waveguide top width, etching depth and the thin-film thickness affect the nominal poling period and the device performance consistency. The inverted ferroelectric domains and the poling defect

NATURE PHOTONICS LETTERS

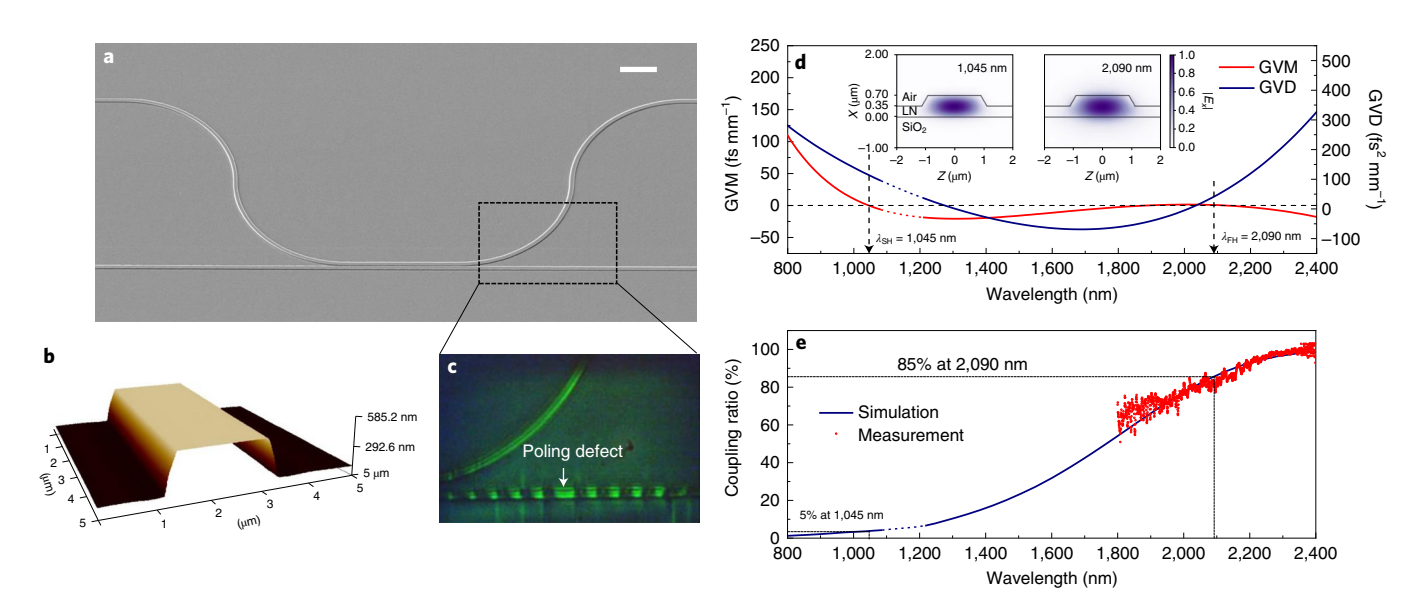


**Fig. 2 | Integrated nonlinear splitter and its linear optical characteristics. a**, SEM image of the fabricated nonlinear splitter. Scale bar, 20 μm. The device has a 2.5-mm-long SHG region and a 3.5-mm-long DOPA region. The directional coupler has a coupling length of 70 μm and a gap of 650 nm between the waveguide top surfaces. **b**, 2D AFM scan of the LN waveguide. **c**, SH microscope image showing the inverted domains and the poling defect along the waveguides. **d**, Simulated GVM (red) between the FH and SH and GVD (blue) for the quasi-transverse electric (quasi-TE) modes of the dispersion-engineered LN waveguide. The optimized waveguide has a top width of 1,650 nm, an etching depth of 350 nm and a total thin-film thickness of 700 nm. The waveguide exhibits low (0.4 fs mm<sup>-1</sup>) GVM between the pump at 1,045 nm and the signal around 2,090 nm, and low GVD for both wavelengths. Inset: electric field distributions of the fundamental quasi-TE modes for the dispersion-engineered waveguide at 1,045 nm and 2,090 nm. The black dashed line in the main plot denotes zero GVM. Black dashed arrows mark the FH and SH wavelengths. **e**, Measured (red symbols) and simulated (blue solid curve) outcoupling ratio of the directional coupler as a function of the wavelength. In **d** and **e**, the dotted lines correspond to the regime where mode crossing between the fundamental TE mode and the second-order transverse magnetic mode occurs, which is distant enough from the SH central wavelength and is not expected to affect the device operation.

along the main waveguide are shown in the SH image in Fig. 2c. Based on the simulation shown in Fig. 1e, the device is designed to have a 2.5-mm-long SHG region and a 3.5-mm-long DOPA region. Such a design can ensure that both the SHG and DOPA process are efficient enough, which in turn leads to low switching energy and high switching contrast in the on state.

To achieve ultralow-energy and ultrafast operation, we engineer the dispersion of the LN ridge waveguide and minimize both the group velocity dispersion (GVD) and the group velocity mismatch (GVM) between the FH and the SH24. Negligible GVD at the FH and SH wavelengths preserves the temporal confinement of these pulses and hence their high peak intensities along the waveguide, thereby ensuring efficient short-pulse and low-energy SHG and DOPA. Additionally, negligible GVM between the FH and SH waves guarantees that both FH and SH pulses travel together along the waveguide. As shown in Fig. 2d, in the dispersion-engineered waveguide, the fundamental quasi-transverse electric (TE) modes at the FH (2,090 nm) and SH (1,045 nm) have a very low GVM of 0.4 fs mm<sup>-1</sup>. In addition, the GVD for both the FH and SH waves are as low as  $40\,\mathrm{fs^2\,mm^{-1}}$  and  $114\,\mathrm{fs^2\,mm^{-1}}$ , respectively. For a 46-fs-long input pulse at 2,090 nm, the optimized waveguide has a dispersion length of more than 50 mm. The walk-off length (pulse length divided by GVM), representing the propagation distance after which the pump and SH pulses acquire a temporal separation equal to their pulse width, is 115 mm. Remarkably, Fig. 2d also shows that, around 2,090 nm, there exists a large wavelength window within which the GVM is close to zero. Therefore, choosing the operating wavelength to be around 2,090 nm can ensure reliably achieving low GVM in the presence of fabrication imperfections.

To ensure that the coupling ratio of the directional coupler is resilient to fabrication errors, we adopt an adiabatic design in which the main waveguide is uniform with a fixed width, while the coupler waveguide width is adiabatically tapered<sup>30</sup>. The detailed geometry of the directional coupler is discussed in Supplementary Section II. Figure 2e shows the wavelength-dependent coupling ratio, which is the ratio between the output power at the drop port and the input power. Owing to the large mode area difference between the fundamental TE modes at 2,090 nm and 1,045 nm, the 70-μm-long directional coupler exhibits a large coupling ratio of over 85% for wavelengths beyond 2,090 nm and a small coupling ratio of less than 5% for wavelengths below 1,045 nm. The measured (red symbols) results around 2,090 nm agree well with the simulation results (blue solid curve). We did not perform the coupling ratio measurement around 1,045 nm because the external input light can be coupled to higher-order spatial modes around 1,045 nm, which strongly affects the accuracy of the measurements.

We characterized the nonlinear optical behaviour of the device using 46-fs-long pulses at 2,090 nm from a synchronously pumped degenerate optical parametric oscillator (OPO) with a repetition frequency of 250 MHz. The characterization of the 2,090-nm pulses is elaborated in Supplementary Section III. By measuring the nonlinear splitter devices with different poling periods, we found that 5.11  $\mu m$  is the optimal poling period for realizing QPM, which is in good agreement with the theoretical period of 5.08  $\mu m$ . The experimental details of optimizing the QPM condition are discussed in the Methods and Supplementary Section V. At the optimum QPM condition, we measured the output power of the FH both at the through port and the drop port. The detailed calibration of the input/output coupling loss of our waveguide is discussed in Supplementary Section VI.

As shown in Fig. 3a, the normalized transmittance from the input to the drop port, defined as  $10\log(T/T_{P_{\rm in}\to 0})$ , shows a clear reduction (~7 dB) when the on-chip input FH pulse energy increases from 0 to 600 fJ. This behaviour is well captured by the simulation

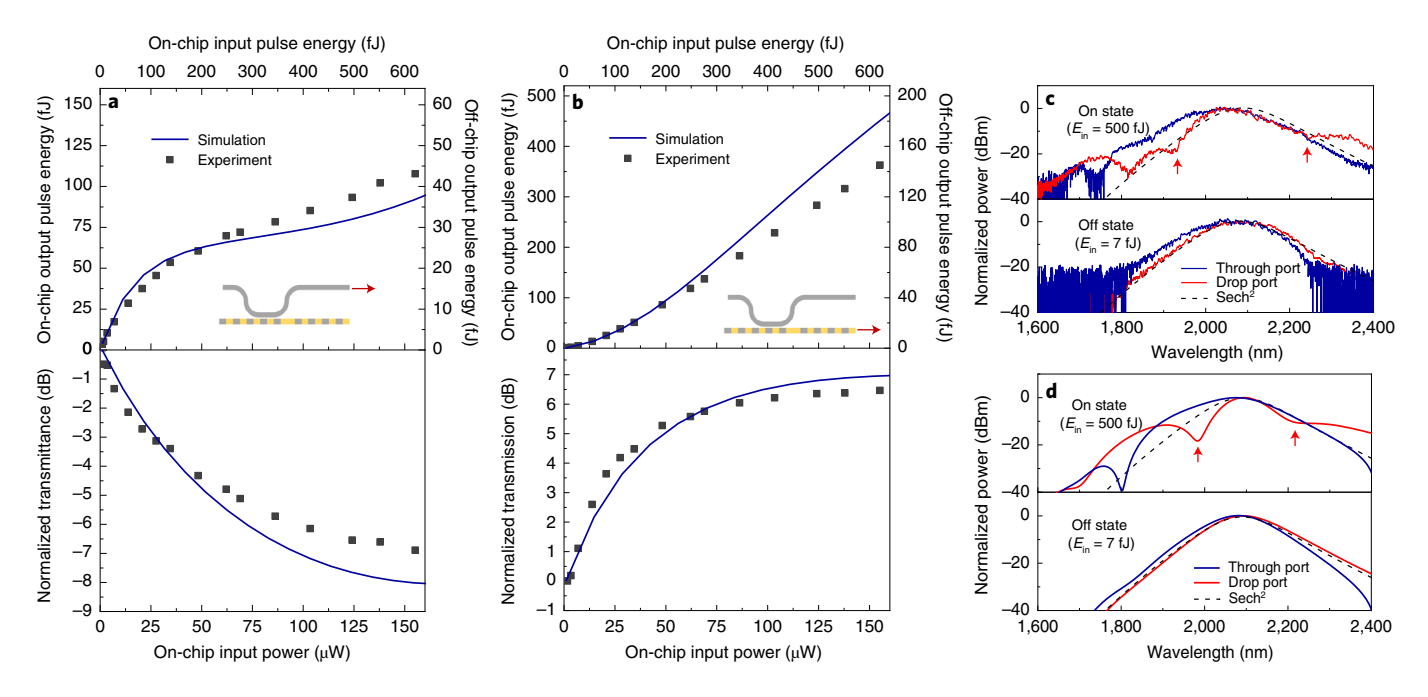


**Fig. 3 | Ultralow-energy nonlinear optical transmission in the integrated nonlinear splitter. a**, Top: output pulse energy of the 2,090-nm FH from the drop port as a function of on-chip input average power/pulse energy. Bottom: normalized transmittance  $(10\log(T/T_{P_{in}\to 0}))$  of the FH from the drop port. **b**, Top: output pulse energy of the FH from the through port as a function of input average power/pulse energy. Bottom: normalized transmittance  $(10\log(T/T_{P_{in}\to 0}))$  of the FH from the through port. In both **a** and **b**, the blue solid lines are simulation results. Black symbols are the measured data. The insets illustrate the ports at which we collected the data. **c**, Measured output FH spectra at the through port (blue) and the drop port (red) in the on state (top) and the off state (bottom). The input FH pulse energy is  $500\,\mathrm{fJ}$  for the on state and  $7\,\mathrm{fJ}$  for the off state. In the on state, the dip in the spectrum of the drop port, which does not persist in the through port or in the off state, is further strong experimental evidence for the interplay of SHG and DOPA in the switching mechanism. **d**, Simulated output FH spectra at the through port (blue) and the drop port (red) in the on state (top) and the off state (bottom), corresponding to the measurements in **c**. In both **c** and **d**, the spectral dips are labelled by red arrows.

(blue solid line). Such a reduction in the transmittance is a result of the strong depletion of FH waves during the SHG process, because the directional coupler only couples out the FH in the first half of the main waveguide. The time-domain nonlinear dynamics of the SHG process is elaborated in Supplementary Section VIII. Because the energy is conserved during the frequency conversion process, based on the measured 7 dB (80%) depletion of the FH shown in Fig. 3a and assuming that the propagation loss of the FH is far less than its depletion, we estimated that an input FH pulse energy of 600 fJ in the waveguide converts to a SH pulse energy of 480 fJ.

The normalized transmittance of the FH from the input port to the through port increases by more than 5 dB as the input pulse energy increases, as shown in Fig. 3b. This behaviour is opposite that of the transmittance to the drop port, which confirms that the poling defect indeed switches the SHG to the DOPA process in the second half of the main waveguide, thereby converting the generated SH back into the FH. The experimental result agrees well with the simulation (blue solid line), despite showing a slightly lower peak transmittance, which can be ascribed to the slightly lower SHG efficiency in the first half of the device or the imperfect phase shift imposed by the poling defect. Based on the results shown in Fig. 3a,b, we can deduce that the largest parametric gain in the DOPA region is more than 12 dB at an input FH pulse energy of 600 fJ, which translates to a gain per unit length of 34 dB cm<sup>-1</sup> given that the DOPA region is 3.5 mm long. Notably, this result is consistent with our recent parametric gain measurement on a similar QPM LN waveguide, which exhibits a gain per unit length of 35 dB cm<sup>-1</sup> when pumped with ~500-fJ, 1,045-nm pulses<sup>24</sup>. Moreover, the measured output FH power from the main waveguide agrees well with the simulation.

The interplay of SHG and DOPA in the all-optical switching mechanism is also evident from the output spectra. In Fig. 3c we

compare the measured output FH spectra at the drop port and the through port. Ultrashort pulses from mode-locked lasers often have a temporal/spectral shape that can be described with a squared hyperbolic secant (sech2) function. When the device is subjected to 500 fJ of input pulse energy (in the on state), the output spectrum at the drop port (red) deviates from the initial sech<sup>2</sup> spectral shape, showing spectral dips around 1,920 nm and 2,250 nm, which indicate a strong depletion of the FH. However, the output spectrum at the through port (blue) does not show such dips at high input pulse energies and has a spectral shape similar to the sech<sup>2</sup> function, which indicates the recovery of the FH power. When the device is in the off state (Fig. 3c, bottom panel), the output spectra measured at the through port and the drop port both have sech<sup>2</sup> shapes because of the weak nonlinear conversion in the off state. Similar behaviours can also be seen in the simulated output spectra for the on state (Fig. 3d, top panel) and the off state (Fig. 3d, bottom panel). In Supplementary Section VIII we provide a detailed analysis of the nonlinear dynamics that explains the origin of the spectral dips. We also explain how the spectral dips are indicative of the power flow direction. The slight difference between the simulated and the experimental spectra can be attributed to a slight difference of pulse shapes after the depletion in the temporal domain due to complexities such as the chirp of the input pulses, the group delay dispersion accumulated along the waveguide propagation, or the non-zero GVM between the FH and SH. It is worth noting that when the input pulse energy exceeds 600 fJ, the input FH exhibits substantial spectral broadening during the SHG<sup>23</sup>, and the phase relation between the FH and SH changes. This leads to a lower parametric gain of the DOPA (details are presented in Supplementary Section VIII).

We further characterize the all-optical switching dynamics and the switching energy of the nonlinear splitter device using NATURE PHOTONICS LETTERS

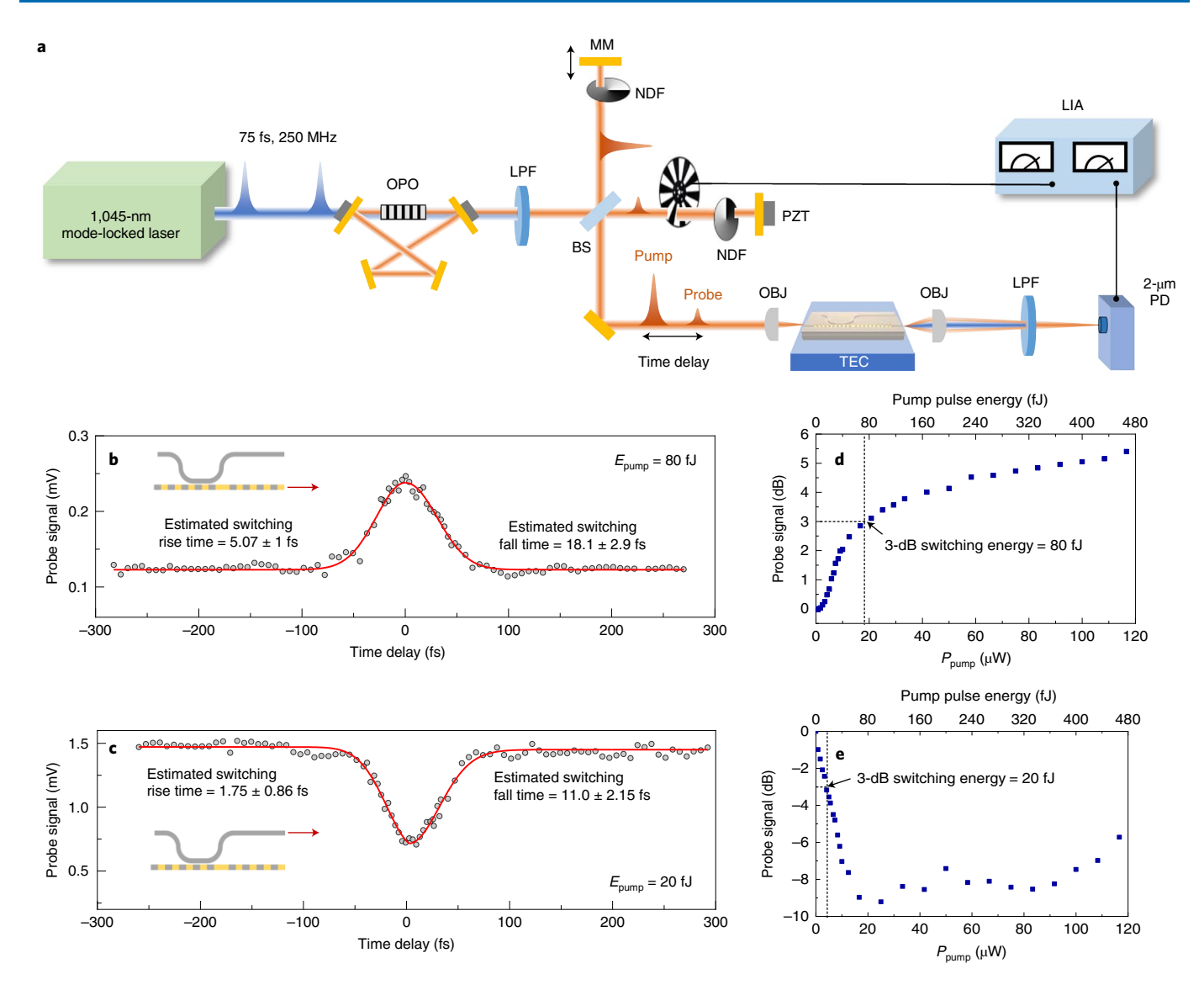


**Fig. 4** [Femtosecond, femtojoule all-optical switching. a, Experimental set-up for the femtosecond all-optical switching measurement. Approximately 46-fs pulses at 2,090 nm generated from a free-space OPO are used to characterize the device. Pump and probe fields with relative time delay  $\Delta \tau$  are injected into the waveguide via the objective lens. Probe transmission depends on whether the two pulses excite the device simultaneously or at different times. LPF, long-pass filter; MM, motorized mirror; PZT, piezoelectric transducer; NDF, neutral density filter; BS, beamsplitter; OBJ, objective lens; LIA, lock-in amplifier; PD, photodetector. **b**, Measured dynamics of the on state at the through port. The input pump pulse energy ( $E_{pump}$ ) is 80 fJ. **c**, Measured dynamics of the on state at the drop port.  $E_{pump}$  is 20 fJ. The insets illustrate the ports at which we collected the data. **d**, Relative probe signal power at the through port as a function of pump pulse power (energy). **e**, Relative probe signal power at the drop port as a function of pump pulse power (energy). The 3-dB switching energies at the through port and the drop port are 80 fJ and 20 fJ, respectively.

a degenerate pump-probe technique, similar to the measurement technique used in ref. <sup>18</sup> As shown in Fig. 4a, a beam containing ~46-fs-long pulses centred at 2,090 nm generated from a table-top degenerate OPO<sup>31</sup> is split into two beams by a beamsplitter in a Michelson interferometer. One beam with a weak optical fluence (3 fJ, 770 nW on-chip average power) is used as the probe beam, and another beam with a high/tunable optical fluence and adjustable time delay (controlled by a motorized delay stage) is used as the pump beam. In the measurement, we couple the output of the Michelson interferometer, which contains both pump and probe beams, to our chip, and switch the transmission of the probe signal by controlling the power of the pump pulse. Additionally, we employ the lock-in modulation and demodulation scheme at 80 Hz to acquire the output probe signal only, rather than acquiring both the pump and probe signals. To suppress the interference between

the pump and probe beams, we use a piezoelectric transducer in the optical path of the probe and modulate the phase of the probe pulses at  $350\,\mathrm{Hz}$ , which is much faster than the integration time (1 s) of the lock-in amplifier.

The dynamics of the on state for the probe signal is measured at the through port and the drop port as plotted in Fig. 4b,c, respectively. At the through port, we observe that the probe pulse is clearly appearing when the pump pulse temporally overlaps with it, whereas at the drop port the probe pulse is eliminated. To extract the rise and fall times of the switching mechanism, we fitted the data with exponential growth and decay functions for relative time delays  $\Delta \tau < 0$  fs and  $\Delta \tau > 0$  fs, respectively, convolved with the autocorrelation of the input pulse, which was approximated by a Gaussian profile with a full-width at half-maximum of 65.2 fs (Supplementary Section III provides details). For the measurement at the through port

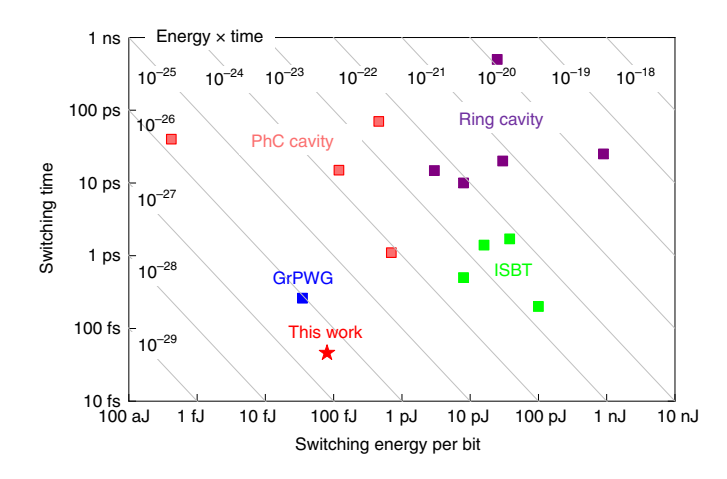


**Fig. 5 | Performance comparison of various on-chip all-optical switches operating at room temperature.** The data points show the intrinsic switching time and switching energy per bit for switches based on a photonic-crystal (PhC) cavity, ring cavity, inter-subband transition (ISBT) and graphene loaded plasmonic waveguide (GrPWG). Our device features a state-of-the-art on-chip switching time of ~46 fs and a low switching energy-time product of  $3.7 \times 10^{-27} \, \text{J} \, \text{s}$ . The references in this plot are included in Supplementary Section IX.

(Fig. 4b), the best fit yields a switching rise time of  $5.1\pm1$  fs and a fall time of  $18.1\pm2.9$  fs. The measurement at the drop port shows a switching rise time of  $1.75\pm0.86$  fs and a fall time of  $11.0\pm2.15$  fs.

Although, in our current experiment, the switching time is limited by the exit pulse length of 46 fs, our results in Fig. 4b indicate that the intrinsic switching time (or response speed) of our device is  $\sim$ 18 fs. This means that if the input pulses have fall times shorter than 18 fs, the switch will not operate efficiently and will distort the pulses at the output. Despite the instantaneous quadratic nonlinearity, the entire all-optical switch still has a finite response time due to the non-zero GVM, GVD and the finite QPM bandwidth, making switching for shorter pulses challenging. We have confirmed with numerical simulations that the asymmetry in the switching dynamics shown in Fig. 4b,c could be caused by the interplay of several dispersion mechanisms, such as GVM and GVD.

The measured ultrafast switching also indicates that the slow dynamics commonly observed in LN and other materials, such as the photorefractive effect<sup>32</sup> and the photothermal effect<sup>33</sup>, are absent, primarily due to the low photon energies of the input FH and the generated SH, the ultralow input pulse energy and the non-resonant nature of the switch. We have also ruled out the intensity-dependent index change (Kerr effect) of the LN waveguide as the possible mechanism for the switching and nonlinear transmission characteristics<sup>34</sup>, given the fact that no switching behaviour and power-dependent transmission were observed on a similar device without poling in the main waveguide.

Figure 4d,e shows the extinction ratio between the on and off states of the switch for both output ports at  $\Delta \tau$ =0. We estimated a switching pump energy of 80 fJ (20 fJ) for the through port (the drop port) at the 3-dB contrast level. Within 500 fJ of input pulse energy, we obtain a switching contrast of over 5 dB in the through port and a switching contrast of over 8 dB in the drop port. Such a high switching contrast is difficult to realize using the saturable absorption in semiconductors<sup>10</sup> and low-dimensional materials<sup>35-37</sup> without coupling them to optical cavities, because it, in general, requires very high optical fluence to excite a substantial portion of electrons from the valence band to the conduction band. It is worth noting that the extinction ratio of our device can be further enlarged to be more than 10 dB at low energy by engineering the coupling ratio of the directional coupler (see Supplementary Section X for details).

In summary, we have demonstrated on-chip all-optical switching based on the strong instantaneous nonlinear response of an LN nano-waveguide, with simultaneous dispersion and QPM engineering. In Fig. 5 we compare our device with existing on-chip all-optical switches in terms of the intrinsic switching time and the switching energy. Our device features a fastest switching time of ~46 fs, corresponding to the largest operational bandwidth of 9.6 THz, as well as an ultralow 3-dB switching energy of 80 fJ. Moreover, our device shows the state-of-the-art switching energytime product of  $3.7 \times 10^{-27}$  J s. Our nonlinear splitter also enables the simultaneous realization of switch-on and switch-off operations as well as a large extinction ratio of over 5 dB when subjected to less than 500 fJ of input pulse energy. Moreover, although our current device is designed for operation at 2,090 nm, the same concept can be applied to telecommunication wavelengths such as 1,550 nm. In Supplementary Section XI, we describe the waveguide design and dispersion engineering for 1,550 nm. Operating the device at a shorter wavelength can also reduce the required lengths for the poling regions due to a larger effective nonlinearity<sup>38</sup>.

We envision that the femtojoule switching energy and the terahertz bandwidth of our all-optical switch can enable new opportunities for terabit per second (Tbps) all-optical information processing in optical time-division multiplexing (OTDM) systems for communication and computing. In Supplementary Section XII we describe the potential applications of our switch for energy-efficient Tbps channel demultiplexing and channel insertion, which are challenging tasks for conventional all-optical switches with more than picosecond switching times. In addition, our switch can also directly interface with the recently developed LN-based on-chip pulsed light sources, such as Kerr soliton microcombs<sup>39-41</sup> and electro-optical combs<sup>42</sup> for on-chip ultrafast information processing<sup>43</sup>. As another important application, our device can serve as an energy-efficient and ultrafast mode-locking element for developing chip-scale mode-locked lasers on TFLN that can generate ~100-fs ultrashort pulses (Supplementary Section XII). The ultrahigh speed, low-energy operation and the larger modulation depth of our device are essential for ultrashort pulse generation, self-starting mode-locking and long-term stability of the generated laser pulses.

# Online content

Any methods, additional references, Nature Research reporting summaries, source data, extended data, supplementary information, acknowledgements, peer review information; details of author contributions and competing interests; and statements of data and code availability are available at https://doi.org/10.1038/s41566-022-01044-5.

Received: 30 August 2021; Accepted: 22 June 2022; Published online: 28 July 2022

## References

- Nozaki, K. et al. Sub-femtojoule all-optical switching using a photonic-crystal nanocavity. Nat. Photon. 4, 477–483 (2010).
- Wetzstein, G. et al. Inference in artificial intelligence with deep optics and photonics. Nature 588, 39–47 (2020).
- Ashtiani, F., Geers, A. J. & Aflatouni, F. An on-chip photonic deep neural network for image classification. *Nature* 606, 501–506 (2022).
- Shtyrkova, K. et al. Integrated CMOS-compatible Q-switched mode-locked lasers at 1,900 nm with an on-chip artificial saturable absorber. Opt. Express 27, 3542–3556 (2019).
- Singh, N., Ippen, E. & Kärtner, F. X. Towards CW modelocked laser on chip—a large mode area and NLI for stretched pulse mode locking. Opt. Express 28, 22562–22579 (2020).
- Grinblat, G. et al. Ultrafast sub-30-fs all-optical switching based on gallium phosphide. Sci. Adv. 5, eaaw3262 (2019).
- Yang, Y. et al. Femtosecond optical polarization switching using a cadmium oxide-based perfect absorber. Nat. Photon. 11, 390–395 (2017).
- Iizuka, N., Kaneko, K. & Suzuki, N. All-optical switch utilizing intersubband transition in GaN quantum wells. *IEEE J. Quantum Electron.* 42, 765–771 (2006).

NATURE PHOTONICS LETTERS

- Takahashi, R., Kawamura, Y. & Iwamura, H. Ultrafast 1.55 μm all-optical switching using low-temperature-grown multiple quantum wells. *Appl. Phys. Lett.* 68, 153–155 (1996).
- 10. Spühler, G. et al. Semiconductor saturable absorber mirror structures with low saturation fluence. *Appl. Phys. B* **81**, 27–32 (2005).
- Almeida, V. R. et al. All-optical switching on a silicon chip. Opt. Lett. 29, 2867–2869 (2004).
- Tanabe, T. et al. Fast all-optical switching using ion-implanted silicon photonic crystal nanocavities. Appl. Phys. Lett. 90, 031115 (2007).
- Hu, X., Jiang, P., Ding, C., Yang, H. & Gong, Q. Picosecond and low-power all-optical switching based on an organic photonic-bandgap microcavity. *Nat. Photon.* 2, 185–189 (2008).
- Martínez, A. et al. Ultrafast all-optical switching in a silicon-nanocrystal-based silicon slot waveguide at telecom wavelengths. Nano Lett. 10, 1506–1511 (2010).
- Yanik, M. F., Fan, S., Soljačić, M. & Joannopoulos, J. D. All-optical transistor action with bistable switching in a photonic crystal cross-waveguide geometry. Opt. Lett. 28, 2506–2508 (2003).
- Chai, Z. et al. Ultrafast all-optical switching. Adv. Opt. Mater. 5, 1600665 (2017).
- Taghinejad, M. & Cai, W. All-optical control of light in micro-and nanophotonics. ACS Photonics 6, 1082–1093 (2019).
- Ono, M. et al. Ultrafast and energy-efficient all-optical switching with graphene-loaded deep-subwavelength plasmonic waveguides. *Nat. Photon.* 14, 37-43 (2020)
- Wang, C. et al. Ultrahigh-efficiency wavelength conversion in nanophotonic periodically poled lithium niobate waveguides. Optica 5, 1438–1441 (2018).
- Zhao, J. et al. Shallow-etched thin-film lithium niobate waveguides for highly-efficient second-harmonic generation. Opt. Express 28, 19669–19682 (2020).
- Chen, J.-Y. et al. Ultra-efficient frequency conversion in quasi-phase-matched lithium niobate microrings. Optica 6, 1244–1245 (2019).
- Rao, A. et al. Actively-monitored periodic-poling in thin-film lithium niobate photonic waveguides with ultrahigh nonlinear conversion efficiency of 4,600% W<sup>-1</sup> cm<sup>-2</sup>. Opt. Express 27, 25920–25930 (2019).
- Jankowski, M. et al. Ultrabroadband nonlinear optics in nanophotonic periodically poled lithium niobate waveguides. Optica 7, 40–46 (2020).
- Ledezma, L. et al. Intense optical parametric amplification in dispersion-engineered nanophotonic lithium niobate waveguides. Optica 9, 303–308 (2022).
- Jankowski, M. et al. Quasi-static optical parametric amplification. Optica 9, 273–279 (2022).
- Schiek, R., Solntsev, A. & Neshev, D. Temporal dynamics of all-optical switching in quadratic nonlinear directional couplers. *Appl. Phys. Lett.* 100, 111117 (2012).
- DeSalvo, R. et al. Self-focusing and self-defocusing by cascaded second-order effects in KTP. Opt. Lett. 17, 28–30 (1992).

 Schiek, R. All-optical switching in the directional coupler caused by nonlinear refraction due to cascaded second-order nonlinearity. *Opt. Quantum Electron.* 26, 415–431 (1994).

- Gallo, K., Assanto, G., Parameswaran, K. R. & Fejer, M. M. All-optical diode in a periodically poled lithium niobate waveguide. *Appl. Phys. Lett.* 79, 314–316 (2001).
- Guo, X., Zou, C.-L. & Tang, H. X. 70-db long-pass filter on a nanophotonic chip. Opt. Express 24, 21167–21176 (2016).
- Marandi, A., Ingold, K. A., Jankowski, M. & Byer, R. L. Cascaded half-harmonic generation of femtosecond frequency combs in the mid-infrared. *Optica* 3, 324–327 (2016).
- 32. Jiang, H. et al. Fast response of photorefraction in lithium niobate microresonators. *Opt. Lett.* **42**, 3267–3270 (2017).
- Ryckman, J. D. et al. Photothermal optical modulation of ultra-compact hybrid Si-VO<sub>2</sub> ring resonators. Opt. Express 20, 13215–13225 (2012).
- Finlayson, N. et al. Picosecond switching induced by saturable absorption in a nonlinear directional coupler. Appl. Phys. Lett. 53, 1144–1146 (1988).
- Li, W. et al. Ultrafast all-optical graphene modulator. Nano Lett. 14, 955–959 (2014).
- Bao, Q. et al. Atomic-layer graphene as a saturable absorber for ultrafast pulsed lasers. Adv. Funct. Mater. 19, 3077–3083 (2009).
- Set, S. Y., Yaguchi, H., Tanaka, Y. & Jablonski, M. Laser mode locking using a saturable absorber incorporating carbon nanotubes. *J. Light. Technol.* 22, 51–56 (2004).
- Jankowski, M., Mishra, J. & Fejer, M. M. Dispersion-engineered χ<sup>(2)</sup>
  nanophotonics: a flexible tool for nonclassical light. *J. Phys. Photon.* 3, 042005
  (2021).
- 39. He, Y. et al. Self-starting bi-chromatic LiNbO $_3$  soliton microcomb. Optica 6, 1138–1144 (2019).
- Gong, Z., Liu, X., Xu, Y. & Tang, H. X. Near-octave lithium niobate soliton microcomb. Optica 7, 1275–1278 (2020).
- 41. Gong, Z. et al. Soliton microcomb generation at 2 μm in z-cut lithium niobate microring resonators. *Opt. Lett.* **44**, 3182–3185 (2019).
- 42. Zhang, M. et al. Broadband electro-optic frequency comb generation in a lithium niobate microring resonator. *Nature* **568**, 373–377 (2019).
- Bogaerts, W. et al. Programmable photonic circuits. Nature 586, 207–216 (2020).

**Publisher's note** Springer Nature remains neutral with regard to jurisdictional claims in published maps and institutional affiliations.

Springer Nature or its licensor holds exclusive rights to this article under a publishing agreement with the author(s) or other rightsholder(s); author self-archiving of the accepted manuscript version of this article is solely governed by the terms of such publishing agreement and applicable law.

 $\circledcirc$  The Author(s), under exclusive licence to Springer Nature Limited 2022, corrected publication 2022

## Methods

**Device fabrication.** We fabricated the nonlinear splitter devices on a 700-nm-thick X-cut MgO-doped LN thin film on 2-μm-thick SiO $_2$  on top of a LN substrate (NANOLN). We first patterned the poling electrodes (15-nm Cr/55-nm Au) with varied electrode finger periodicities using electron-beam lithography. The electrodes were then formed by electron-beam evaporation and metal liftoff. We performed the ferroelectric domain inversion (periodic poling) by applying several 380-V, 5-ms-long pulses at room temperature with the sample submerged in oil. We visually inspected the poling quality using a SH microscope. Next, we removed the electrodes by wet chemical etching, and patterned the waveguides using electron-beam lithography. The pattern was transferred to the LN layer by Ar $^+$  plasma etching. Finally, the waveguide facets were polished to enable good light-coupling efficiencies.

Optical measurements. For the linear and nonlinear optical measurements, we employed a free-space light-coupling set-up, as shown in Fig. 4a. The 1,045-nm source is a 1-W Yb mode-locked laser that produces nearly transform-limited 75-fs-long pulses at a 250-MHz repetition rate (Menlo Systems Orange). The output 1,045-nm beam was fed into a near-synchronously pumped degenerate OPO44 to produce ~46-fs-long pulses centred at 2,090 nm. Detailed characterization of the 2,090-nm pulses is discussed in the Supplementary Section III. The output 2,090-nm beam was split into two beams by a beamsplitter in a Michelson interferometer. The two beams were then recombined and coupled into the nonlinear splitter chip by a reflective objective (Newport 50102-02). The average off-chip input power was calibrated by a thermal power meter (Thorlabs PM16-401). The input/output coupling losses at 2,090 nm were estimated to be 21.6 dB/4 dB. For the power-dependent transmittance measurements in Fig. 3, only one output beam from the Michelson interferometer was used. The chip was placed on a thermoelectric cooling stage. To adjust the QPM condition, temperature tuning was used (Supplementary Section V). For the results in Fig. 3a,b, the output power was measured by an optical spectrum analyser covering 1,200-2,400 nm (Yokogawa AQ6375B) with a 2-nm-resolution bandwidth. For the result in Fig. 4b-e, the output power was measured by an IR 2-µm photoreceiver (Newport 2034).

Numerical simulations. We used commercial software (Lumerical) to solve for the waveguide modes as well as to obtain the dispersion characteristics shown in Fig. 2c. In the simulation, the anisotropic index of the LN was modelled by the Sellmeier equations<sup>45</sup>. For the nonlinear optical simulation, we solved an analytical nonlinear envelope equation in the frequency domain using a split-step Fourier technique to simulate the pulse propagation and nonlinear dynamics in the waveguide<sup>46</sup>. The nonlinear step was solved with a fourth-order Runge–Kutta method. Details regarding the single-envelope simulation are provided in Supplementary Section IV.

# Data availability

The data that support the plots within this paper are available at https://figshare.com/s/6fb22ae146577d1ac7c0.

## Code availability

The computer code used to perform the nonlinear simulations in this paper is available from the corresponding author upon reasonable request.

#### References

- 44. Jankowski, M. et al. Temporal simultons in optical parametric oscillators. *Phys. Rev. Lett.* **120**, 053904 (2018).
- Zelmon, D. E., Small, D. L. & Jundt, D. Infrared corrected sellmeier coefficients for congruently grown lithium niobate and 5 mol.% magnesium oxide-doped lithium niobate. J. Opt. Soc. Am. B 14, 3319–3322 (1997).
- 46. Phillips, C. et al. Supercontinuum generation in quasi-phasematched waveguides. *Opt. Express* **19**, 18754–18773 (2011).

# Acknowledgements

Device nanofabrication was performed at the Kavli Nanoscience Institute (KNI) at Caltech. We thank K. Vahala and C. Yang for loaning equipment. We also thank J.-H. Bahng, R. Briggs and M.-G. Suh for assistance with the fabrication development process. A.M. gratefully acknowledges support from ARO grant no. W911NF-18-1-0285, NSF grants nos. 1846273 and 1918549, AFOSR award no. F49550-20-1-0040 and NASA/JPL. We thank NTT Research for financial and technical support.

## **Author contributions**

Q.G. and A.M. conceived the project. Q.G. fabricated the devices and performed the measurements, with assistance from R.S., R.N., S.J. and R.M.G. L.L. developed the single-envelope simulation tool. L.L., D.J.D. and A.R. contributed to the design of the device. Q.G. and L.L. analysed the experimental results and performed the simulations. L.L. performed the periodic poling. Q.G. wrote the manuscript, with input from all other authors. A.M. supervised the project.

## Competing interests

Q.G. and A.M. are inventors on a patent application (US patent application no. 17/500,425) that covers the concept and implementation of the all-optical switch described here. The remaining authors declare no competing interests.

#### Additional information

**Supplementary information** The online version contains supplementary material available at https://doi.org/10.1038/s41566-022-01044-5.

Correspondence and requests for materials should be addressed to Alireza Marandi.

**Peer review information** *Nature Photonics* thanks the anonymous reviewers for their contribution to the peer review of this work.

Reprints and permissions information is available at www.nature.com/reprints.